Materials Chemistry and Physics 313 (2024) 128665

Contents lists available at ScienceDirect

Materials Chemistry and Physics

journal homepage: www.elsevier.com/locate/matchemphys

Enhancing photocatalysis through annealing: Unveiling the role of physical properties in photocatalytic behavior

B. Tiss [a,b,*], W. Zayoud [b], H.E. Sekrafi [a,c], N. Bouguila [b], D. Cristea [d], C. Croitoru [d], L. Velicu [e], V. Tiron [f], P. Prepelita [g], V. Craciun [g,h], C. Moura [a], L. Cunha [a]

[a] Physics Center of Minho and Porto Universities—CF-UM-UP, University of Minho, Campus de Gualtar, 4710-057, Braga, Portugal
[b] Laboratory of Physics of Materials and Nanomaterials Applied at Environment, Faculty of Sciences in Gabes, Gabes University, 6072, Gabes, Tunisia
[c] Laboratoire de Physique des Matériaux, Faculté des Sciences de Sfax, Université de Sfax, B.P. 1171, 3000, Sfax, Tunisia
[d] Materials Science and Engineering Faculty, Transilvania University, Eroilor 29, 500036, Brasov, Romania
[e] Faculty of Physics, Alexandru Ioan Cuza University of Iasi, 700506, Iasi, Romania
[f] Research Center on Advanced Materials and Technologies, Department of Exact and Natural Sciences, Institute of Interdisciplinary Research, Alexandru Ioan Cuza University of Iasi, 700506 Iasi, Romania
[g] Laser Department, National Institute for Laser, Plasma, and Radiation Physics, Magurele, Romania
[h] Extreme Light Infrastructure for Nuclear Physics, IFIN-HH, Magurele, Romania

HIGHLIGHTS

- In_2S_3:Ag films deposited via spray pyrolysis underwent vacuum annealing at 400 °C.
- The annealing process significantly influenced the physical properties of the samples.
- Optimal crystallite, grain size, and RMS were observed for all the samples with 4 % Ag.
- Samples with 4 % silver content exhibited over 95 % photodegradation efficiency.

ARTICLE INFO

Keywords:
Spray pyrolysis
Annealing
In_2S_3:Ag films
Physical properties
Photocatalytic activity

ABSTRACT

Using spray pyrolysis, silver-doped In_2S_3 thin films were deposited on pre-heated glass substrates, with varying doping concentrations. Subsequently, these films underwent vacuum annealing at 400 °C for a duration of 2 h. A comprehensive study of their structural, morphological, and optical properties was conducted, revealing homogeneous, compact, crack-free films with polycrystalline tetragonal-phase of In_2S_3. Among the set of the analyzed films the best parameter values, including crystallite size, dislocation density, micro-strain, grain size, and root mean square (RMS) roughness, were achieved when maintaining a Silver-to-indium (|Ag|/|In|) ratio of 4 % in the precursors for both as-deposited and annealed samples. The annealing process had a discernible impact on the grain size distribution, resulting in a significant increase in crystallite and grain size, along with RMS roughness, for most doped films. The optical analysis of these films unveiled their transparency in the visible and near-infrared regions, coupled with substantial absorption in the UV region. Higher Ag concentration in the as-deposited films led to an increased band gap energy in the annealed samples. The roughness peaked at |Ag|/|In| = 4 %, resulting in a noteworthy enhancement of photocatalytic activity, achieving 95 % photodegradation of a methylene blue aqueous solution. This underscores the critical role of surface properties in determining performance. Future research intends to explore other applications for these thin films, including potential usage in gas sensors, capitalizing these films' promising characteristics.

1. Introduction

Despite concerns about the problems caused by pollution, particularly water pollution, new forms of pollution are emerging around the world. Recently, a new type of surface water pollution has arisen due to the increased consumption of drugs to treat a growing

* Corresponding author. Physics Center of Minho and Porto Universities—CF-UM-UP, University of Minho, Campus de Gualtar, 4710-057, Braga, Portugal.
E-mail address: sofian.tis15@gmail.com (B. Tiss).

https://doi.org/10.1016/j.matchemphys.2023.128665
Received 5 July 2023; Received in revised form 4 October 2023; Accepted 7 November 2023
Available online 15 November 2023

number of illnesses, including cancer [1–3]. One example is Ifosfamide, an anti-cancer drug that is partially processed by the body and is found in large quantities in hospital effluents [4]. Research has shown that degradation of Ifosfamide by advanced oxidation processes (AOP), such as photocatalysis under ultraviolet (UV) radiation, is efficient. However, using metal oxides in photocatalysis under solar irradiation reduces efficiency because these materials can only be activated by UV radiation due to their high energy band gap (E_g) [5]. Fast recombination of charges and restricted activation to UV radiation limit photocatalysis with metal oxides [6,7]. Other low bandgap semiconductors overcome these problems, making the photocatalytic process more efficient under solar irradiation [8–10]. Low bandgap semiconductors are used in various applications, such as photovoltaic cells and screens [8–10]. Indium sulfide (In_2S_3) semiconductor films are an alternative to cadmium-based films for creating a solar cell structure with metal oxides [11–13]. In_2S_3 is a n-type III-VI chalcogenide semiconductor [14]. It has a direct band gap energy of 2.0–3.0 eV and high transparency [15–17]. At atmospheric pressure, In_2S_3 has three allotropic forms, α, β and γ, with phase transitions occurring at 420 °C and 754 °C [18]. The β-In_2S_3 phase is the most thermodynamically stable and exhibits excellent optoelectronic performance [19], making it a good photocatalyst and photosensitizer [20–22]. Different types of β-In_2S_3 micro/-nanostructures, such as nanoparticles, nanoflakes, nanosheets, nanorods, nanotubes, microspheres, thin films and hollow nanostructures, have been synthesized using various methods [23–31]. β-In_2S_3 thin films have been deposited by physical and chemical vapor deposition methods, such as spray pyrolysis, sputtering, chemical bath deposition, electroplating, etc. [26]. Among these methods, spray pyrolysis has the advantage of being simple, easy to handle, and cost-effective for large surfaces. However, sprayed β-In_2S_3 thin films have a high resistivity, which must be reduced for certain applications [32–34]. Doping and heat treatment can reduce electrical resistivity [35]. In the literature, several metallic elements are referred as dopants of In_2S_3 [36–39]. Among these elements, copper (Cu) and silver (Ag) are easily diffused into In_2S_3, affecting its lattice structure, and consequently its physical properties [40]. Silver has been chosen as a dopant for In_2S_3 thin films due to its luminescence properties [41] and its antiseptic properties [42,43]. Studies [44–48] have shown that Ag doping has a significant effect on the physical properties of indium sulfide, namely on the crystal structure, morphological and electrical properties, reducing the electrical resistance of In_2S_3. The annealing process, which rearranges atoms into equilibrium positions and reduces stress on the crystal lattice, is crucial in improving physical properties [49–53]. Crystalline quality and surface roughness, which are important parameters in photocatalytic performance, are also affected by annealing [51,54,55]. Several authors are working on the thermal oxidation of indium sulfide, and they have found that at temperatures close to 400 °C, indium oxide crystals start to be detected [56,57]. These results reported by other groups inspired our group to work with this annealing temperature (400 °C), under a certain level of vacuum, to ensure the absence of secondary phases potentially caused by the thermal oxidation of In_2S_3. Therefore, this study presents results related to silver-doped indium sulfide thin films deposited by spray pyrolysis with varying concentrations of silver dopants, heat-treated under vacuum at 400 °C for 2 h. The resulting samples were analyzed using physical characterization techniques to correlate the physical properties with the photocatalytic activity.

2. Experimental details

The silver-doped indium sulfide films utilized in this study were obtained through a two-step process. The first step involved depositing the films onto glass substrates using spray pyrolysis at a substrate temperature of 350 °C. Three precursors, namely indium chloride ($InCl_3$), thiourea ($SC(NH_2)_2$), and silver nitrate ($AgNO_3$), were used to produce the films. The sample preparation protocol is presented extensively, elsewhere [58]. Five films were produced, each one with varying Ag concentration. The identification of the samples and the ratio of Ag to In atomic concentration in the precursor solution during films production, labeled as "|Ag|/|In| (%)", are documented in Table 1.

The second preparation step corresponds to seal the five films in Pyrex tubes, under medium vacuum (2×10^{-2} mbar) and to anneal them at 400 °C, for 2 h. The variation of the temperature during the annealing process is represented in Fig. 1.

The obtained samples were analyzed by several characterization methods in order to better correlate the physical properties/characteristics with their photodegradation potential of a methylene blue (MB) dye solution. To analyze the structure of these films, an EMPYREAN X-ray diffractometer from Malvern Panalytical, with CuKα X-ray source, was used. The diffraction patterns were analyzed using the Panalytical software package HighScore Plus™ and the ICDD 2020 database.

To estimate the average crystallites size and micro-strain, the Williamson Hall method was used [59]:

$$\boldsymbol{\beta \cos \theta = \frac{k\lambda}{D} + 4\varepsilon \sin \theta} \quad (1)$$

where β, θ, λ and ε are the full width at half maximum (FWHM), the diffraction angle, the X-ray wavelength and the micro-strain, respectively. The shape factor is represented by k, and a typical value of 0.9 was used. The dislocation density (δ) is a measure of the number of dislocations per unit volume (an estimation of the crystalline quality) and is calculated based on the following equation [60]:

$$\boldsymbol{\delta = \frac{1}{D^2}} \quad (2)$$

In order to analyze the morphology, the roughness and the thickness of the deposited films, atomic force microscopy (AFM) and scanning electron microscopy (SEM) were used. The AFM equipment was a Solver Pro-M system from NT-MDT, and the analysis was performed in air, at room temperature, in non-contact mode (NC-AFM). Random zones were scanned, and the generated images were processed using the Nova software.

The SEM equipment was an Inspect S50 microscope from ThermoFisher Scientific FEI. The cross sectional and top view SEM images of the films were acquired at an electron acceleration voltage of 20 kV, and with a lateral resolution of ~2 nm. The thin film samples were mounted on a conductive substrate, a conductive tape was used, from the top surface of the sample to the sample holder, in order to dissipate charging. Furthermore, the samples were coated by magnetron sputtering (Magnetron AGAR 108 Auto) with a gold thin film (8 Å - 15 Å) in order to reduce the static charge on the surface during the analysis. The optical characterization was performed with a Shimadzu UV-3101 PC spectrophotometer.

To assess the photodegradation capacity, an aqueous solution of methylene blue was prepared, with a concentration (c_{init}) of 10^{-5} M and a pH = 6.5. The absorption spectrum of the solution was obtained, and each of the five samples was immersed in 10 mL of the solution. The photocatalytic behavior was studied by placing the solutions with the samples in a closed cylindrical reactor, at a room temperature of 22 °C. Four lamps, located on the walls of the reactor, emitted in the visible region of the electromagnetic spectrum. Before starting the irradiation, 20 μL of 30 % wt. H_2O_2 was added to each solution. After 4.5 h of irradiation, the solutions with the samples were removed from the reactor and a new set of absorption spectra of the solutions was

Table 1
Identification of the as-produced samples, |Ag|/|In| atomic ratio in the precursors during production.

Sample ID	T1V	T2V	T3V	T4V	T5V
$Ag/_{In}$ (%)	0	2	4	6	8

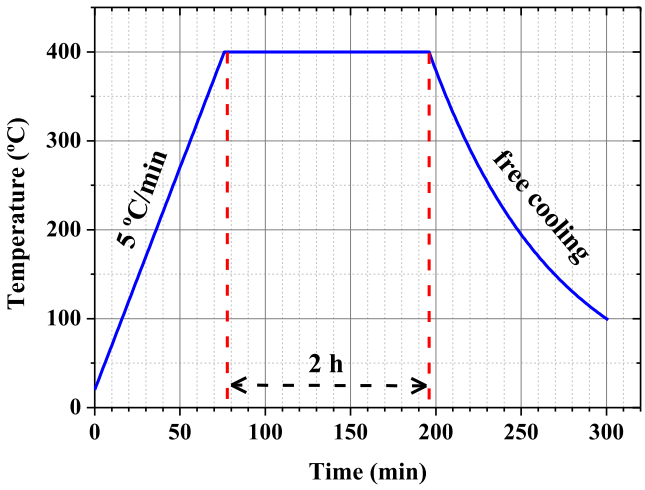

Fig. 1. Temperature profile of the annealing treatment ($T(t)$).

obtained. The spectra were collected by a Dynamica Halo XB-10 spectrophotometer. The photodegrdadation efficiency (η) was estimated using the following equation (3):

$$\eta = \frac{C_{init} - C_{fin}}{C_{init}}.100(\%) \quad (3)$$

where c_{fin} is the final MB concentration in each solution.

3. Results and discussions

3.1. Microstructure

SEM micrographs of the films reveal similar morphology and thickness (around 1.2 μm). Fig. 2 exhibits the cross section of one of the films (T3V). The films are free of cracks or holes, but the cross-section and the observed part of the surface, also reveal the presence of grains.

Atomic Force Microscopy (AFM) micrographs offer qualitative and quantitative information of the films' surface. Using P9 (IA-P9) software, the root mean square (RMS) roughness and average grain size

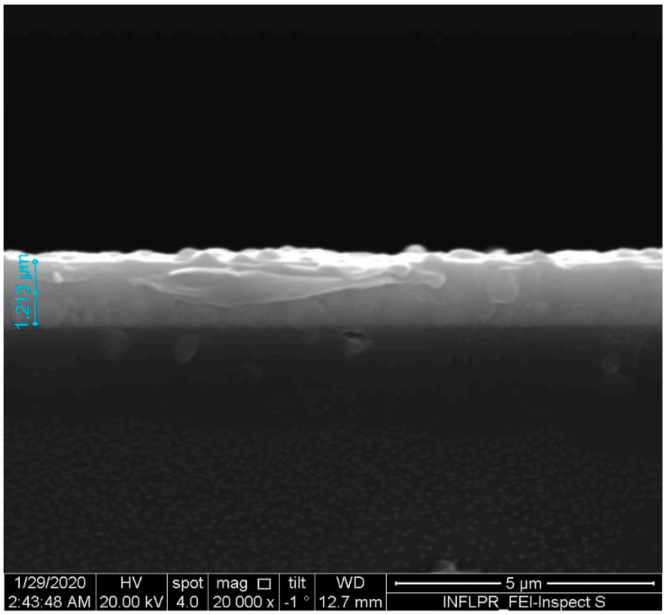

Fig. 2. Cross section SEM micrograph of a representative film (T3V).

were estimated. The 2D and 3D micrographs of the as-deposited and the vacuum annealed In_2S_3:Ag thin films are presented in Fig. 3(A,a - E,e). The surface morphology of a material is an important characteristic that can significantly affect its physical and chemical properties. The obtained images provide crucial insights into the surface characteristics of both as-deposited and annealed samples. Notably, the images reveal that all samples exhibit continuous surfaces, well-covered, homogeneous, compact, and free of any visible cracks or holes. Moreover, the effect of the annealing process on the surface morphology of the as-deposited films is noticeable, particularly in the 3D AFM images. It is evident that the annealing process has an impact on the surface features of the material, causing changes in its topography and texture. Interestingly, the surface properties of the films are also significantly influenced by the silver doping effect, which is apparent in both the 3D and 2D AFM images. These findings suggest that both the annealing and silver doping affect the morphology of the films' surface, highlighting the importance of carefully controlling these factors in material design and engineering.

The grain size distribution histograms presented in Fig. 4(A,a - E,e) provided valuable insights into the material's microstructure. Based on these histograms, several key parameters were extracted and are summarized in each histogram. The impact of both doping and annealing on the surface properties of the films is clearly evident from the extracted parameters presented in Fig. 4. Specifically, it can be observed that the central position (x_c) correspondent to the most frequent grain size, full width at half maximum (FWHM), and height (y_{max}) of the fitting peaks, changes upon increasing the silver doping and also upon subsequent annealing. Excepting the as-deposited and the annealed film without Ag, that presents a Gaussian-type of grain size distribution, all the other films exhibit a higher dispersion of grain sizes, evidenced by grains sizes centered around multiple dimensions. Apparently, the Ag doping causes grains growth in sizes around 2 to 5 different dimensions (multicentered grain size distributions). Fig. 5 shows the grain size distribution affected by the doping concentration and by the annealing process. In terms of Ag doping, the average grain size tends to increase until the Ag concentration in the precursors is 4 % and to decrease for higher Ag concentration. The annealing causes a grain size increase regardless of the amount of Ag in the precursors. It also enhances the multicentered grain size distribution.

The values for the average grains size and the roughness of the as deposited and annealed films, as function of the silver content are presented in Fig. 6. The graph clearly shows that the average grain size exhibits a maximum at a 4 % silver concentration, for both as-deposited and annealed samples. Excepting the case of the sample produced with 8 % of Ag doping, upon annealing, the grain size significantly increases. The thermal energy due to the annealing promotes the crystal growth with atoms located in grains boundaries, reduction of structural defects and, although less probable, it may also promote the coalescence of smaller nuclei or neighboring grains, leading to improved crystal quality [61]. The RMS roughness is also affected by the addition of silver. The Ag concentration has a noticeable impact on the surface roughness of the samples, confirming what is observed in the AFM image (Fig. 3). Specifically, the evolution of roughness changes from the as-deposited situation, where it increases as the Ag concentration increases, to the annealed situation, in which the roughness significantly decreases for all the films, except for the film produced with Ag concentration of 4 %. So, the maximum RMS roughness, after annealing, is for the T3V sample ($|Ag|/|In| = 4$ %). The roughness of the films potentially promotes the enhancement of the photocatalytic performance [62].

3.2. Structural analysis

Fig. 7 depicts the X-ray diffraction patterns obtained from the annealed In_2S_3:Ag thin films, providing evidence of their polycrystalline nature. The cubic (ICDD card no. 00-032-0456) and tetragonal (ICDD card no. 04-007-5233) phases of indium sulfide are difficult to distinguish, but the cubic phase is less probable [18], so it is assumed that the

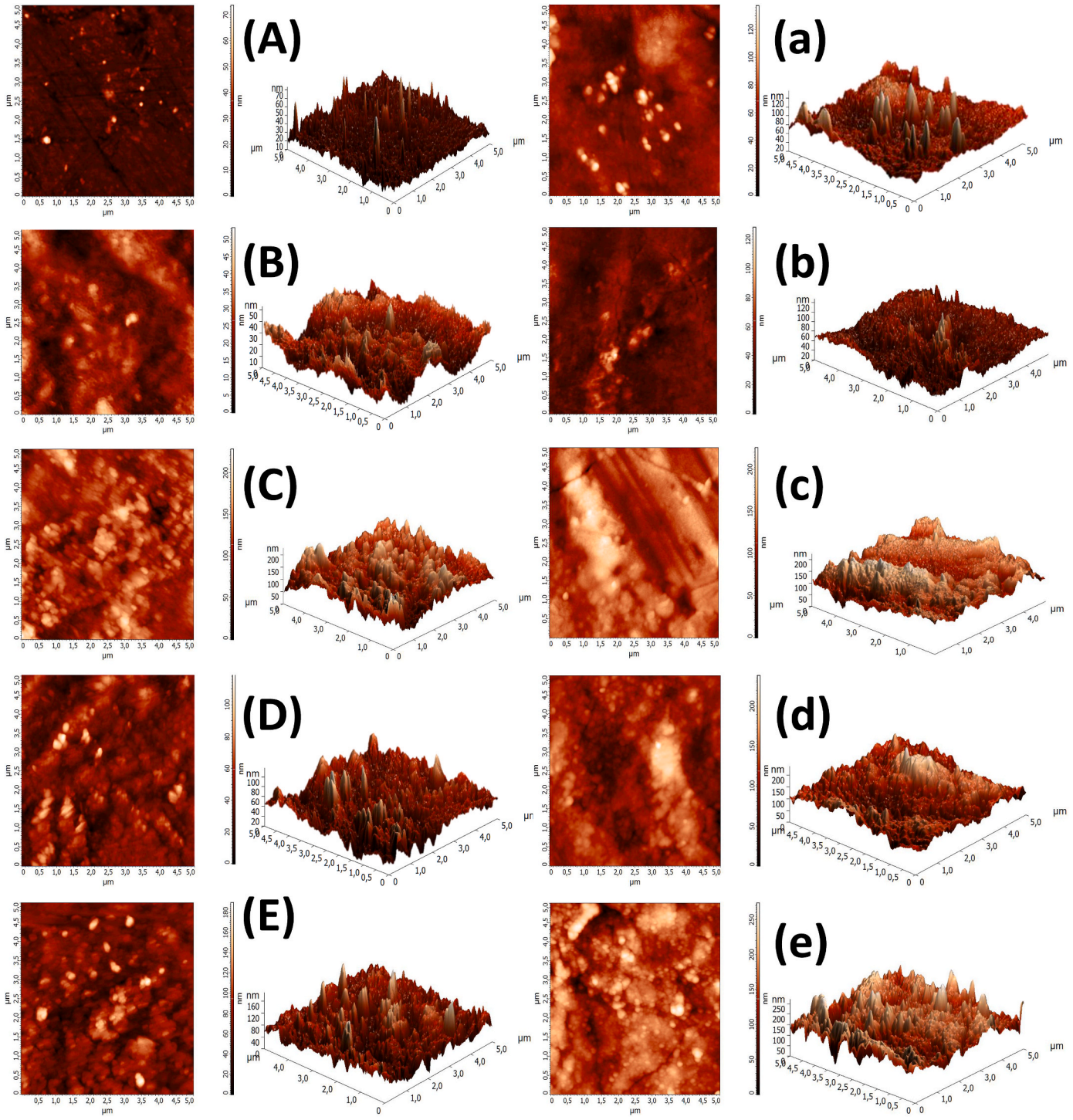

Fig. 3. 2D, 3D (NC)-AFM micrograph of the as deposited (capital letter) and annealed (small letters) samples for different Ag doping concentration: (A, a) 0 %, (B, b) 2 %, (C, c) 4 %, (D, d) 6 %, (E, e) 8 %.

films exhibit crystallization of the tetragonal phase of β-In_2S_3, regardless of the dopant concentration. The addition of Ag, within the limits of this work, did not significantly affect the crystal structure of the In_2S_3 thin films. The four most intense peaks correspond on diffraction on planes (1 0 9) and (2 0 0) at $2\theta \approx 27.5°$, (0 0 12) and (2 0 0) at $2\theta \approx 33.3°$, (3 2 3) and (1 0 15) at $2\theta \approx 43.7°$, and (4 0 0) and (2 2 12) at $2\theta \approx 47.8°$. The peaks correspondent to (0 0 12) and (2 0 0) planes are the most intense regardless the Ag doping amount. The diffraction patterns obtained from the samples do not show indium oxide or silver peaks. This suggests a consistent crystal structure across the samples. In contrast, Tiss et al. [58,63] demonstrated that the most intense crystalline orientation of as-deposited samples changes from when the dopant concentration in the precursors increases from 6 % to 8 %. This suggests that the doping rate may have an effect on the as-prepared samples, but the annealing, under the tested conditions, seems to promote crystalline similarity.

Fig. 8 illustrates the intensity ratios of the XRD peaks for the as-deposited and annealed films. The intensity ratio of the most intense peak, attributed to (1 0 9) and (2 1 3) crystal planes, relative to the second most intense peak, attributed to (0 0 12) and (2 2 0) planes, is plotted in Fig. 8(a). Additionally, the intensity ratio of the most intense

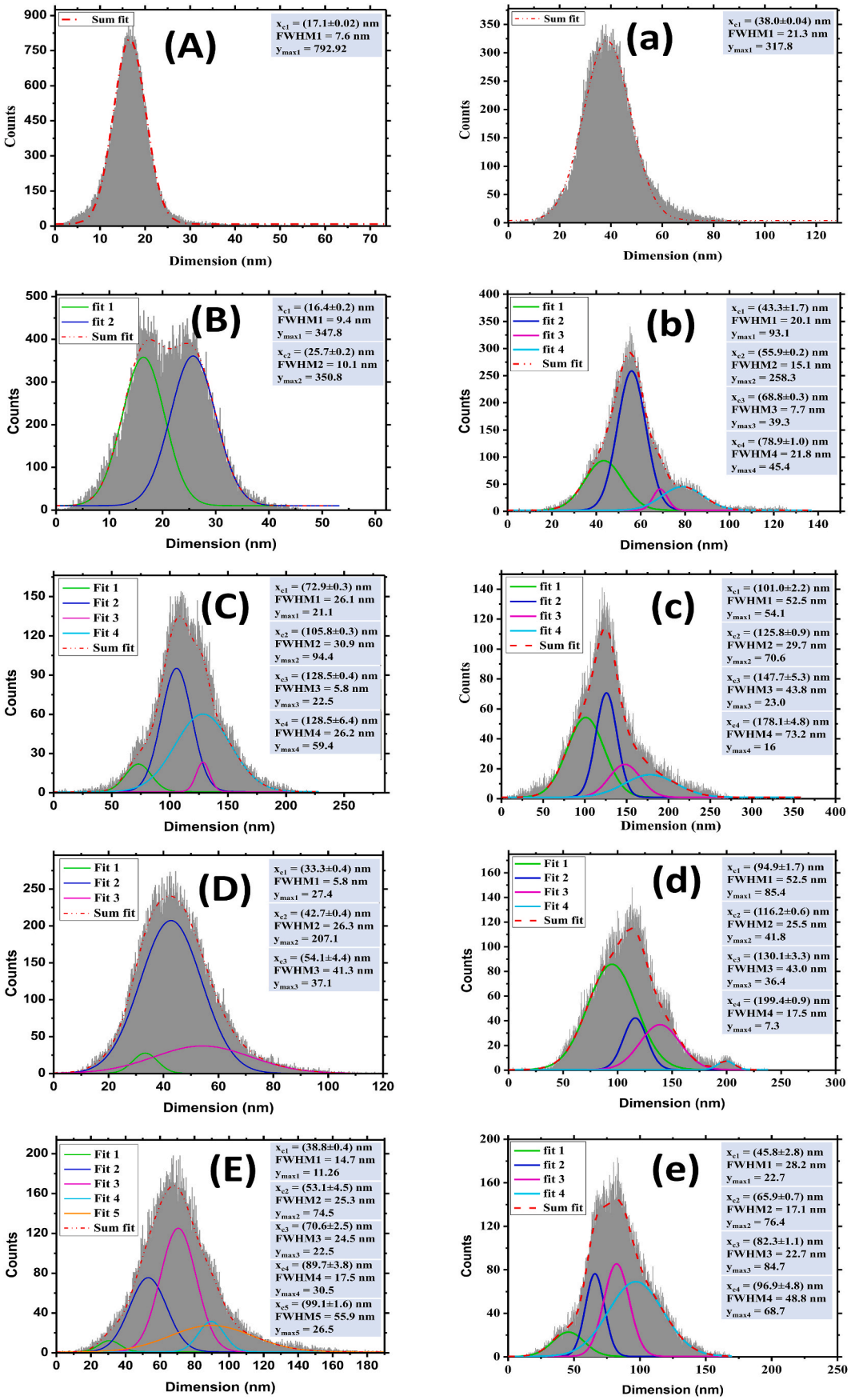

Fig. 4. Grains size distribution of the as deposited (capital letter) and annealed (small letters) samples for different Ag doping concentration: (A, a) 0 %, (B, b) 2 %, (C, c) 4 %, (D, d) 6 %, (E, e) 8 %.

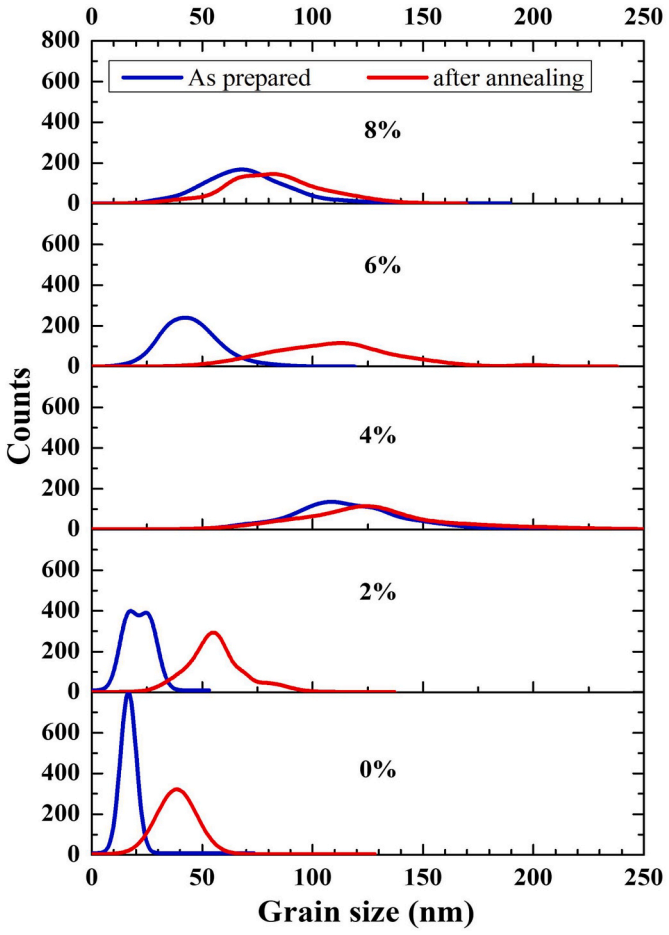

Fig. 5. Comparison of the grains size distribution fitting curves.

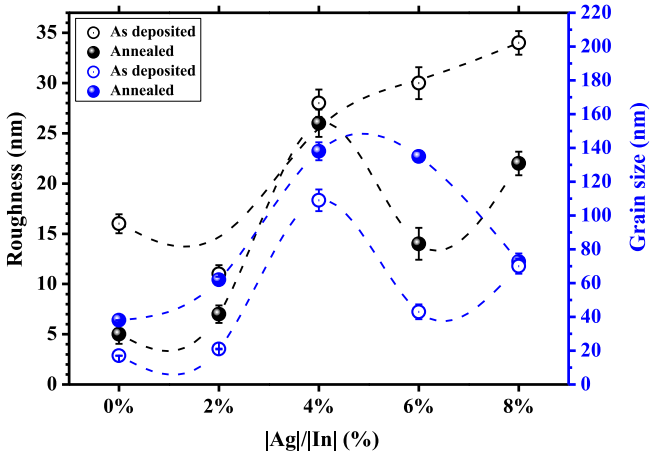

Fig. 6. Roughness and grains size of the as deposited and annealed films.

peak relative to the sum of intensities of all other detected In_2S_3 peaks is presented in Fig. 8(b).

Three important observations can be made from these plots:

i) There is a noticeable decrease of both ratios for the annealed samples, indicating a change in crystal growth behavior due to the thermal treatment;

ii) For both the as-deposited and annealed films, the highest ratios are observed for the T3V film, which was produced with a precursor ratio of |Ag|/|In| = 4 %. However, after annealing, the difference in intensity ratios between the T3V film and the other films diminishes significantly;

iii) In both the as-deposited and annealed states, as depicted in Fig. 8 (a) and **(b)**, the intensity ratios decrease when |Ag|/|In| exceeds 4 %. This suggests that the annealing process has a stronger

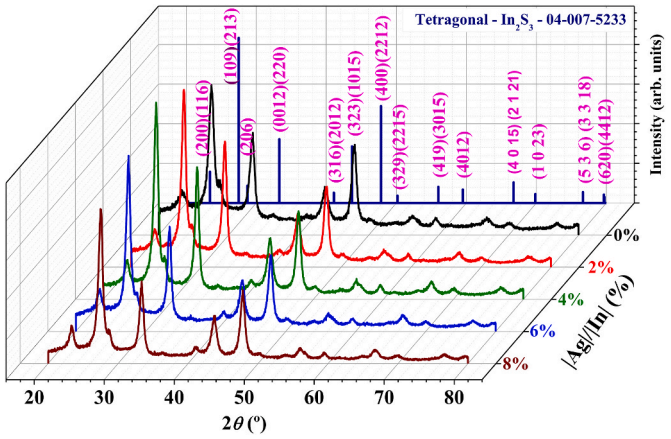

Fig. 7. XRD patterns of the annealed samples.

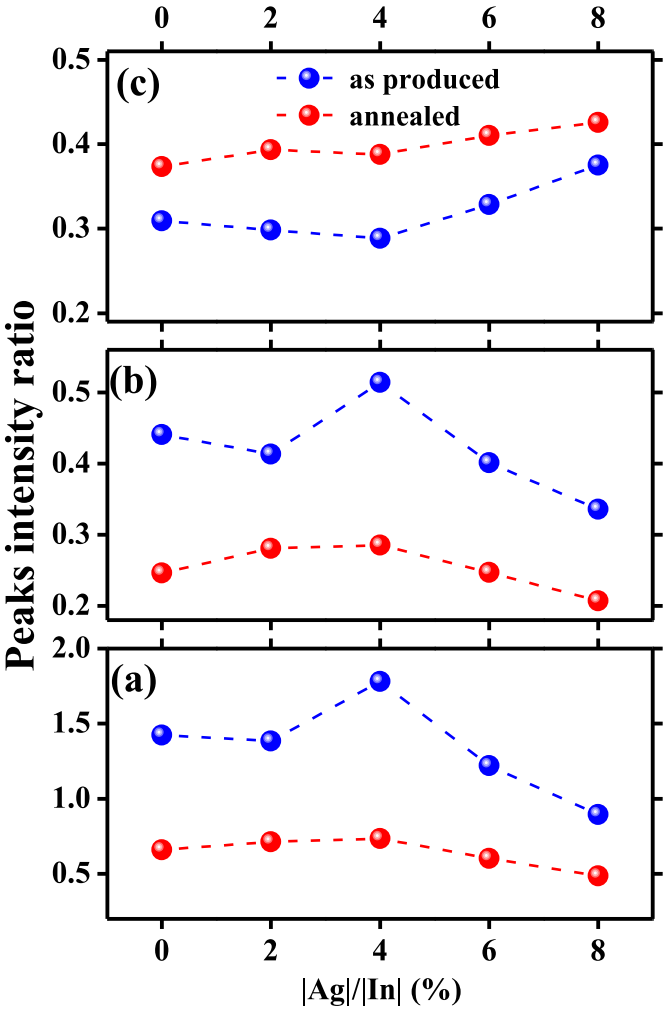

Fig. 8. XRD peaks intensity ratios: (a) [(1 0 9)+(2 1 3)]/[(0 0 12)+(2 2 0)]; (b) [(1 0 9)+(2 1 3)]/All; (c) [(0 0 12)+(2 2 0)]/All.

influence on the film properties compared to the dopant concentration.

Based on these observations, it can be inferred that the annealing effect supersedes the impact of the dopant concentration on the crystal growth behaviour.

When plotting the intensity ratio of the second most intense peak, attributed to the (0 0 12) and (2 2 0) crystal planes, divided by the sum of intensities of all the other detected peaks ((Fig. 8(c)), the observed trend is nearly opposite to that shown in Fig. 8(b). In this scenario, annealing leads to an increase in the intensity ratio for all films, and the peak intensity ratios exhibit an upward trend when |Ag|/|In| exceeds 4 %.

To conclude the analysis of Fig. 8, although there are peaks with a relatively high intensity, there is no evidence of a preferential direction of crystal growth during deposition, but the annealing treatment appears to induce a tendency towards homogenization regarding the crystal growth directions, despite the fact that, when the |Ag|/|In| ratio in the precursors is 4 %, it seems to be a pivotal concentration.

Annealing usually improves the crystalline quality of the samples [64] and it should have consequences in the crystallite size (D). The five most intense peaks of the XRD patterns in Fig. 7 were used to calculate the average crystallites size, as well as the micro-strain, by plotting ($\beta \cos\theta$) as a function of 4 $\sin\theta$. The corresponding graphs are summarized in Fig. 9 for all the films, in the situation of as-produced (in red), and after annealing (in blue).

From these plots, it is evident that the sample with |Ag|/|In| = 4 %, stands out from the rest. In Fig. 9, it is verified that when |Ag|/|In| < 4 %, the ($\beta \cos\theta$) values for all (4 $\sin\theta$) points after annealing, are consistently lower than those of the as-deposited samples. Conversely, when |Ag|/|In| > 4 %, the opposite is true. When the Ag/In ratio is 4 % (T3V), a mixed situation is observed. Thus, when |Ag|/|In| = 4 %, there is a transition between two modes. The slope of the linear fit of the plots of Fig. 9 corresponds to the micro-strain (ε) and the crystallites size (D) is estimated from the ordinate at the origin. The obtained values of D, ε and of the dislocation density (δ) are summarized in Fig. 10.

As a consequence of annealing, it is observed an increase of the estimated crystallites size of In_2S_3:Ag films (Fig. 10(a)). This growth is more significant for samples with no Ag or lower Ag concentration (|Ag|/|In| ≤ 4 %). To quantify the influence of the annealing on the sizes of the crystallites, the variation of the size ΔD ($\Delta D = D_{\text{after annealing}} - D_{\text{as deposited}}$) and relative variation $\Delta D/D_{\text{as deposited}}$ were calculated (Table 2). Despite the T3V film's absolute crystallite growth being the greatest (from 17 nm to 27 nm), the sample with no Ag (T1V) revealed the largest percentage growth. The annealing process is important for promoting the repositioning of the atoms in their equilibrium locations [52]. Upon closer examination, the T3V film (Ag/In = 4 %) exhibits the largest crystallite size (in as-deposited and annealed conditions). However, beyond this doping level, the crystallite size decreases. The shape of the

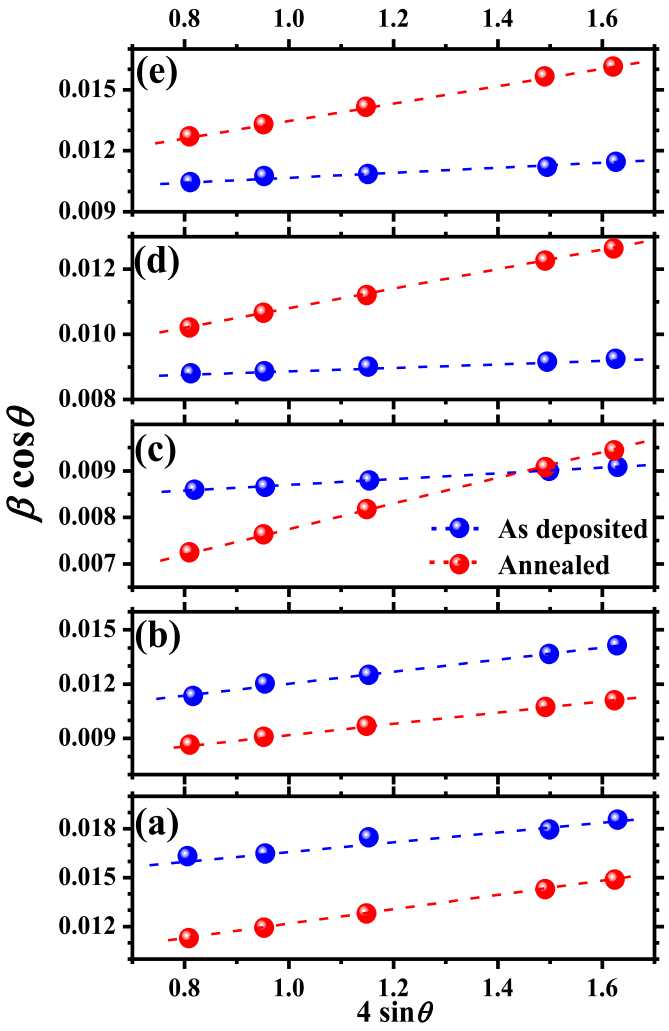

Fig. 9. Williamson Hall plots of all the films: (a) 0 %; (b) 2 %; (b) 4 %; (c) 6 %; (e) 8 %.

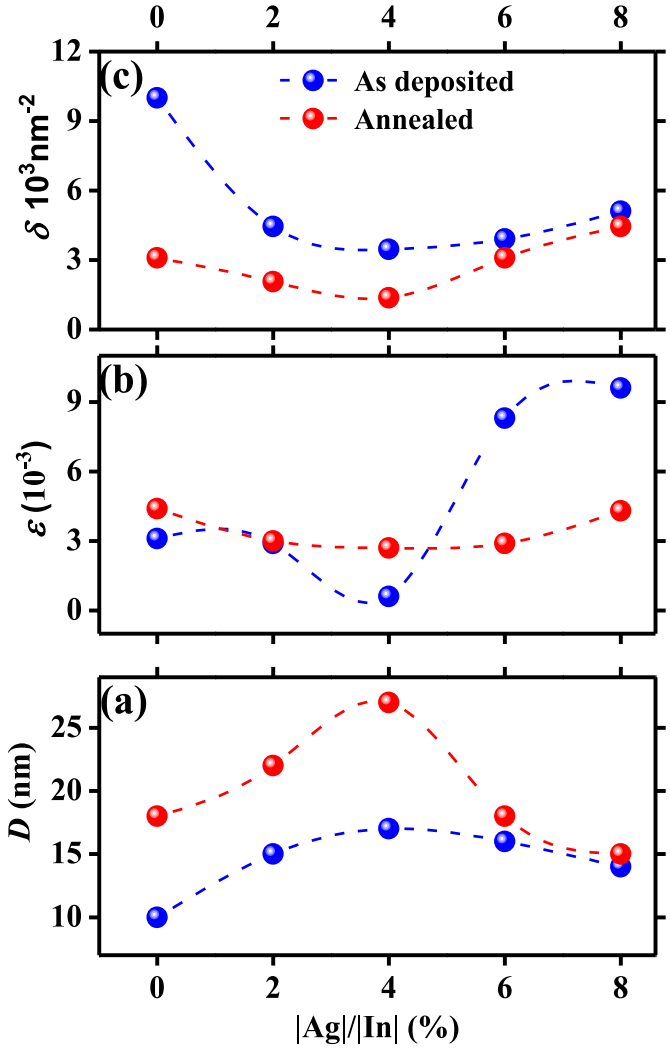

Fig. 10. Variation of the crystallite sizes (a), micro-strain (b) and dislocation density (c), for as-deposited and annealed samples, as function of the Ag doping.

Table 2
Absolute and relative variation of average crystallite size promoted by the annealing treatment.

Sample/$\frac{\lvert Ag\rvert}{\lvert In\rvert}$	ΔD (nm)	$\Delta D/D_{\text{as deposited}}$ (%)
T1V/0 %	8	80
T2V/2 %	7	32
T3V/4 %	10	37
T4V/6 %	2	11
T5V/8 %	1	7

curve (Fig. 10(a)) representing the variation of crystallite size with Ag content for annealed samples, with a maximum for sample T3V, may be attributed to the insertion of Ag (the ionic radius of Ag^{+}: 1.26 Å) into interstitial sites or even to Ag occupying In (the ionic radius of In^{3+}: 0.81 Å) vacancies. For $|Ag|/|In| \leq 4$ %, the increasing Ag content in the as-produced lattice does not impede the increase in crystallite size brought about by annealing. However, when $|Ag|/|In| > 4$ %, the excess Ag appears to accumulate primarily at the crystallite boundaries, not significantly contributing to an increase in grain size but instead hindering crystal growth by incorporating atoms at the boundaries or through coalescence.

Fig. 10(b) illustrates that, prior to annealing, the crystallites of In_2S_3: Ag T3V sample ($|Ag|/|In| = 4$ %), exhibited the lowest strain ($\varepsilon = 0.6 \times 10^{-3} = 0.06$ %). However, as the concentration of $|Ag|/|In|$ exceeded 4 %, the micro-strain underwent a significant increase. This observation suggests that the concentration of silver in the In_2S_3 matrix has a profound effect on the microstructure and consequently on the material properties. Following annealing, the micro-strain values of the samples maintain the same trend as observed before annealing, with the film $|Ag|/|In| = 4$ % displaying the lowest micro-strain value. The micro-strain values show a lower variation with respect to the Ag concentration in the annealed sample compared to the as-deposited sample. This indicates that after the annealing, the Ag concentration provokes minimal changes of the microstructure of the films. Annealing typically causes stress relaxation, which is evident in the annealed samples.

The annealing process improves the quality of all crystallites, with the T3V sample exhibiting the lowest dislocation density (Fig. 10(c)). Through annealing, expected changes in crystalline parameters, within the 0–8% range of $|Ag|/|In|$ in the precursors, are observed. The most favorable outcome is observed at $|Ag|/|In| = 4$ %, where both ε and δ decrease before increasing beyond this point. The opposite variation happens relatively to the evolution of crystallite size. Albeit on a different scale of variation, this evolution is similar to the one displayed by the as deposited samples. Among all examined samples, the T3V film with a $|Ag|/|In| = 4$ % exhibits the highest crystalline quality.

3.3. Optical analysis

In order to examine the optical characteristics of the samples, the transmission (Fig. 11(a)) and absorption (Fig. 11(b)) spectra with respect to wavelength of the incident radiation were acquired, providing a comprehensive picture of their evolution.

These spectra show three distinct zones: an almost zero transmission (high absorption) in the ultraviolet (UV) region of the spectrum (around $\lambda <$ 450 nm), so the material can be used as a UV filter; an edge zone separating the previous zone to a zone with significant transmission (around 450nm $< \lambda <$ 600 nm), fundamental to estimate the band gap energy; a transmission zone (around $\lambda >$ 600 nm) with the presence of interferences fringes. Furthermore, as depicted in Fig. 11, it is evident that the deposited thin films exhibit high transparency within the visible and near-infrared (NIR) regions. Notably, the transmittance significantly increases in the NIR range, reaching approximately 98 % when the wavelength is around 3000 nm. This remarkable level of NIR transmittance renders these films highly suitable for applications that rely on NIR light, particularly in the fields of Photovoltaics [65]. The incorporation of Ag in the indium sulfide films, within the limits of the Ag concentration used in these samples, does not seem to affect significantly their optical behavior, particularly the limits of the referred three zones. In contrast, this result differs from our findings with the as-deposited samples, where it was observed that the Ag doping significantly affected the transmittance. For instance, it was observed that the transmittance reduced from 90 % for $|Ag|/|In| = 4$ %–60 % for $|Ag|/|In| = 8$ % [58]. Nevertheless, the increase of Ag incorporation increases the absorption of radiation with $\lambda <$ 450 nm (Fig. 11(b)). Based on absorption data the absorption coefficient (α) can be estimated by using equation (5) [66]:

$$\alpha = 2.303\frac{A}{d} \tag{5}$$

where d and A are the thickness and absorption, respectively.

Fig. 12(a) shows the evolution of the absorption coefficient as a function of the photon energy in the near infrared (NIR) and visible regions of the electromagnetic spectrum. The absorption coefficient is close to zero in the NIR region and increases significantly in the transition from the NIR to visible regions. The extinction coefficient (Fig. 12 (b)) exhibits a similar behavior, as it was expected from the spectra and from the absorption coefficient. These lower values of α and k indicate the good crystalline quality of the films and are in agreement with the structural results [63].

Based on the absorption coefficient, the bandgap energy (E_g) was estimated using Tauc's law [67]:

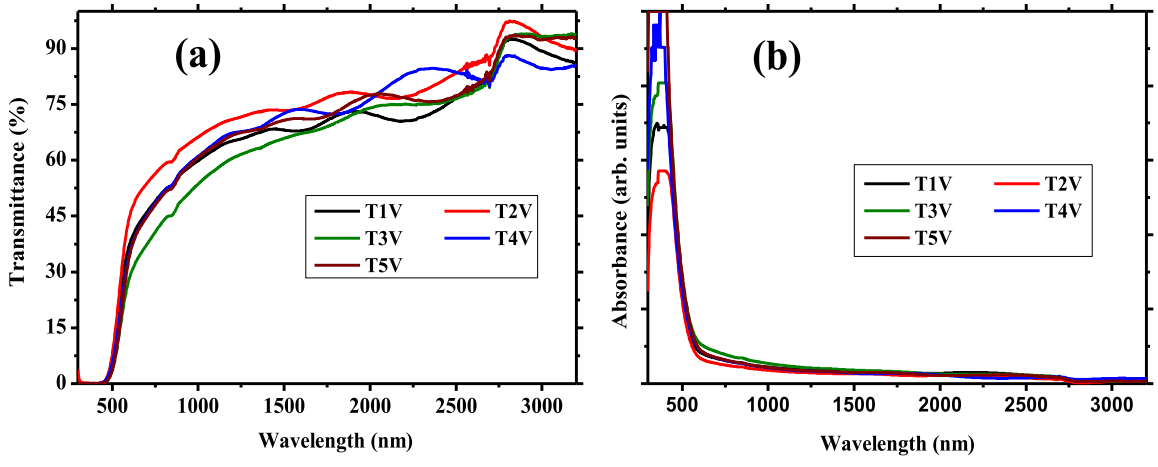

Fig. 11. Optical spectra of the films: (a) transmittance; (b) absorbance, as function of the wavelength.

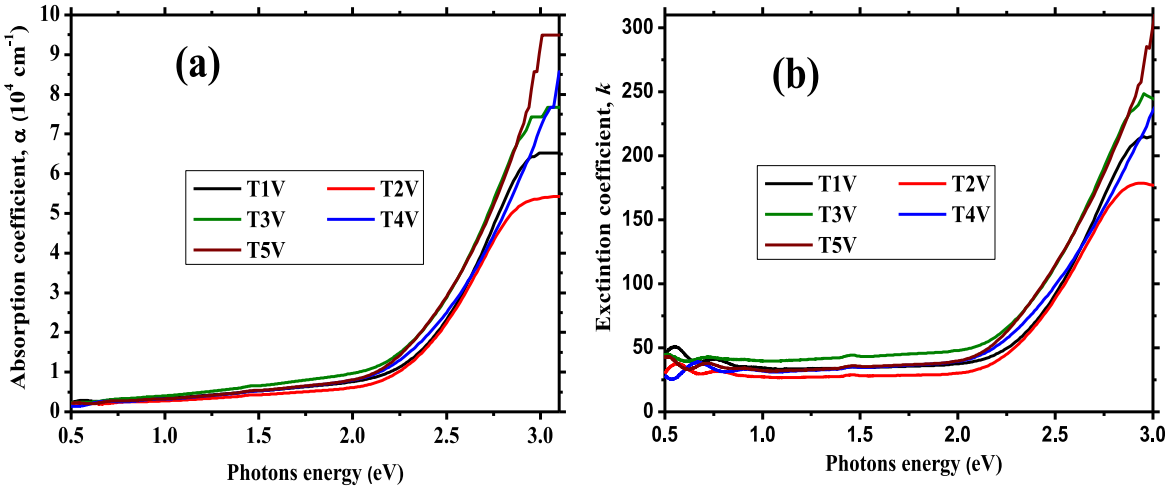

Fig. 12. Evolution of (a) absorption and (b) extinction coefficients as function of the photon energy of the films.

$$(\alpha h\nu)^2 = B(h\nu - E_g) \quad (6)$$

where B is a constant depending on the transition probability and the exponent 2 is related to direct gap of In_2S_3 [15]. The evolution of $(\alpha h\nu)^2$ as a function of $h\nu$ is presented in Fig. 13(a), for sample T1V, without Ag. The intersection of the linear part with the x-axis ($\alpha = 0$) gives a good estimation of E_g. The obtained values of E_g for all samples are illustrated in Fig. 13(b). As it was observed for the as-deposited samples [63], the band gap energy increases with increasing doping concentration. The E_g values of all the samples are in the E_g range of In_2S_3 found in the literature [15–17]. Upon comparison of the band gap energy of the annealed samples with the results reported by Tiss et al. [58,63], it becomes apparent that the band gap energy reduces from the as-deposited to the annealed samples. This observation is consistent with an increase in crystallite size, which can be explained by the quantum confinement effect. As the size of the crystal increases, the electronic states become less confined, resulting in a decrease in the band gap energy. The band gap energy evolution for the annealed samples as function of the doping rate could be explained by the improvement of the crystallinity which leads to the reduction of tails' bands, particularly after the annealing. Another interpretation is related to Burstein-Moss effect (BM) [68] which explains the variation of E_g with the doping concentration: when the semiconductor is heavily doped, the Fermi level can pass into the conduction band (CB).

3.4. Photocatalytic analysis

A 10^{-5}M methylene blue dye solution was used as a model organic pollutant in the photodegradation process facilitated by annealed Ag-doped In_2S_3 coatings. The absorbance spectra of the MB solutions, with and without Ag:In_2S_3 samples, after a total irradiation time of 4.5h, are highlighted in Fig. 14(a).

The spectrum of MB solution presents five characteristic absorption peaks: around 580 nm associated to trimers $(MB^+)_3$; around 610 nm corresponding to dimers $(MB^+)_2$; around 665 nm to monomers MB^+, and around 550 nm and 700 nm corresponding to higher order aggregates or adsorption on other materials [69]. A significant decrease in the maxima of the spectra is clearly observed for the samples that contained the Ag:In_2S_3 samples, compared to the reference sample. This is a clear indicator of the photodegradation capacity of these types of coatings, confirming literature results [70,71].

Another observation is related to the main peak (≈665 nm), which shifts to lower wavelength (hypsochromic effect), possibly due to electron transfer and charge complexes formation. When the dye molecule interacts with the photocatalyst, there can be electron transfer between them, leading to a redistribution of electron density in the dye molecule, resulting in a shift of the absorption peak to higher energy (lower wavelength) [72]. In addition, there is a greater reduction in the peak intensity of the monomer compared to that of the dimer, probably due to a more facile disruption of the energy levels of the monomer species by the photocatalyst. This indicates that the rate of the monomer degradation is superior to that of dimer degradation. This shifting and decreasing of the absorption peak of the monomers' bands are linked to the N-demethylation degradation of MB concomitantly with the phenothiazine degradation [73]. In relation to the amount of silver doping, it is observed that the absorption intensity shows a minimum for

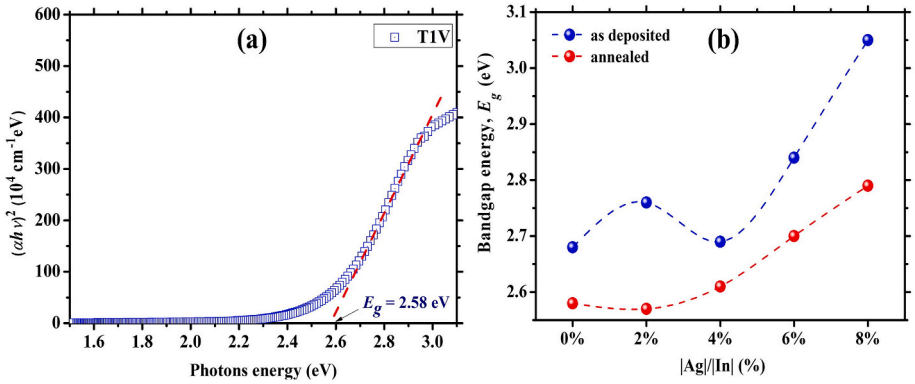

Fig. 13. (a) Band gap energy of the films from plotting of $(\alpha h\nu)^2$ versus photons energy ($h\nu$) for sample T1V; (b) Band gap energy of the films.

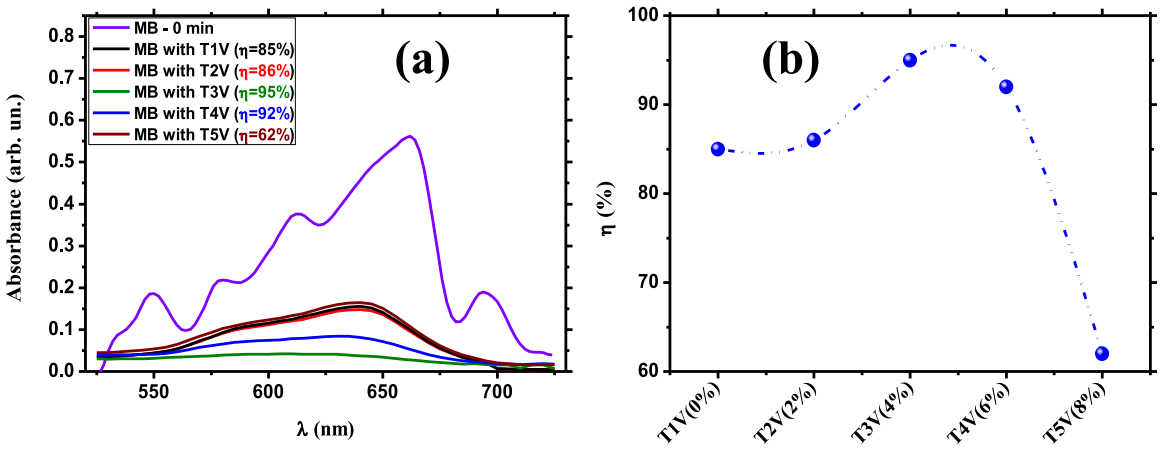

Fig. 14. Photocatalytic tests results: (a) Absorbance spectra of MB solution as a reference and MB solution containing the samples after 4.5h under visible irradiation; (b) Photocatalytic efficiency of the films as function of Ag doping.

film T3V (|Ag|/|In| = 4 %). It is noteworthy to mention that the absorption spectrum of the MB solution containing sample T3V, after being exposed to visible light, is almost a line very close to zero. This observation indicates that MB is almost completely photodegraded in presence of this sample and under the test conditions presented herein. Furthermore, the photodegradation efficiency (η) was estimated by using equation (3), and the obtained values for all the samples are summarized in Fig. 14(b). All the films exhibit significant photodegradation capacity, but the film produced with a |Ag|/|In| ratio of 4 % in the precursors exhibits the highest photocatalytic efficiency in regard to the degradation of the MB solution.

As shown in this figure, the MB photodegradation efficiency evolves in a similar way to other parameters, namely: crystallites, grain size, and RMS roughness, increasing with higher doping concentration, up to |Ag|/|In| = 4 % (film T3V), followed by a depreciation.

The average surface roughness is a key factor influencing the evolution of η. Among the analyzed thin films, T3V exhibits the highest RMS roughness, suggesting its potential as a more effective catalyst, which has indeed been confirmed.

Correlating film roughness, specifically RMS roughness, with photodegradation efficiency, can offer key insights into photocatalytic material performance. Higher RMS roughness signifies a surface with greater irregularities and more pronounced features, leading to a larger surface area-to-volume ratio. This, in turn, offers a greater number of active sites for photocatalytic reactions. This increased surface area often leads to enhanced photodegradation efficiency by facilitating greater pollutant interaction with the photocatalyst. Rough surfaces also scatter light in multiple directions, boosting photon absorption and the generation of vital electron-hole pairs crucial for photocatalytic reactions. Additionally, surface roughness influences charge carrier dynamics, with surface defects or irregularities serving as charge carrier trap sites that promote efficient charge separation, reduce recombination, and enhance photo-generated charge utilization for pollutant degradation. In certain cases, increased roughness correlates with a more widespread distribution of catalytic sites on the surface, further amplifying the material's capacity to catalyze chemical reactions involved in photodegradation [74].

The schematic of the photocatalysis mechanism aided by In_2S_3:Ag is shown in Fig. 15. When In_2S_3 semiconductor receives a photon energy greater than or equal to the band gap energy ($h\upsilon$), electrons (e^-) move towards the conduction band (CB) and the holes (h^+) are generated in the valence band (VB). The following equation can explain this behavior:

$$In_2S_3 + h\upsilon \rightarrow In_2S_3\left(e^-_{CB} + h^+_{VB}\right) \quad (7)$$

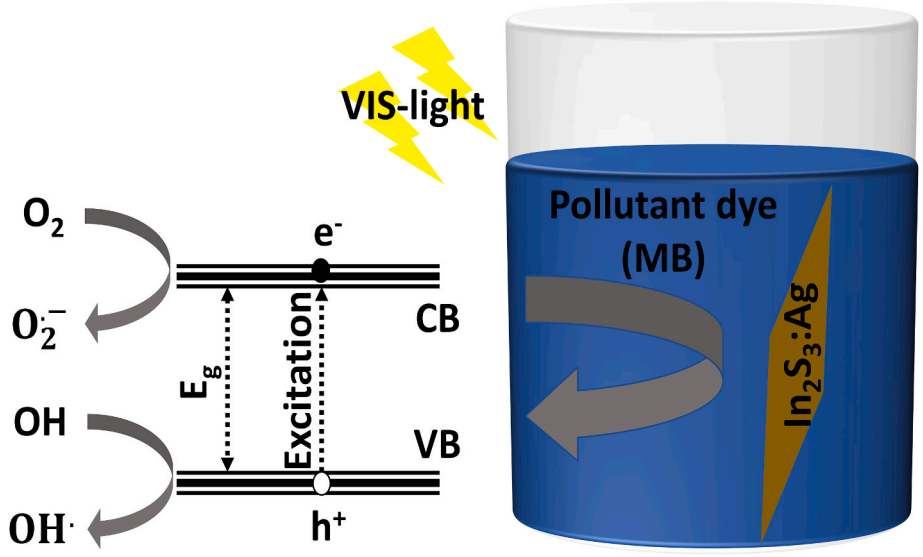

Fig. 15. Schematic MB photodegradation mechanism under visible light.

Thus, positive holes (h^+_{VB}) photo-generated on the surface of this catalyst can cause the oxidation of water molecules or hydroxide ions (OH^-) to produce reactive hydroxyl radicals (·OH).

$$In_2S_3\left(h^+_{VB}\right) + \left(H_2O \leftrightarrow H^+ + \bullet OH\right) \rightarrow In_2S_3 + H^+ + \bullet OH \quad (8)$$

In addition, the electrons located in the CB are captured by the adsorbed oxygen to produce a superoxide radical anion ($\bullet O_2^-$). This later reacts with a proton (e.g., from water) as an additional source of hydroxyl radicals or oxidizing agents to form a hydroperoxyl radical. The electrons in CB are responsible for the generation of hydroxyl radicals which accelerate the degradation of the MB dye as shown in the following equations:

$$MB + \bullet O_2^- \rightarrow \textbf{degradation produced} \quad (9)$$

$$MB + \bullet OH \rightarrow \textbf{degradation produced} \quad (10)$$

4. Conclusions

Silver-doped indium sulfide (Ag:In_2S_3) thin films were synthesized via spray pyrolysis by varying the |Ag|/|In| ratio in the precursor solution from 0 % to 8 % (with a step size of 2 %). The samples were subjected to vacuum annealing at 400 °C for 2 h. Annealing is a process that facilitates the atomic rearrangement, and the films exhibit polycrystalline structure, crystalizing in the tetragonal phase of In_2S_3. Optimal properties, including crystallite size, dislocation density, microstrain, grain size, and RMS roughness, were observed for both as-deposited and annealed samples when the |Ag|/|In| ratio in the precursor was 4 %. Following annealing, a significant increase in crystallite and grain size, as well as RMS roughness, was observed. Optical characterization revealed that the materials exhibited opacity in the ultraviolet range and transparency in the visible and near-infrared regions. Additionally, in the case of as-deposited films, the band gap energy of the annealed samples increased with higher Ag concentrations.

Due to the substantial increase in roughness observed in Ag-doped In_2S_3 films, the sample produced with Ag|/|In| ratio of 4 % demonstrated remarkably high efficiency in photocatalytic activity, achieving an impressive level of 95 %.

Furthermore, these samples possess key attributes, with a particular emphasis on the irregular morphological state of the films' surfaces. This irregularity contributes significantly to the enhanced roughness of the surfaces, increasing the surface area-to-volume ratio. This contributes to a surplus of active sites, thereby amplifying the potential for improved gas-sensing capabilities.

CRediT authorship contribution statement

B. Tiss: Investigation, Writing – original draft. **W. Zayoud:** Writing, Data curation. **H.E. Sekrafi:** Software, Formal analysis. **N. Bouguila:** Conceptualization, Supervision, Resources. **D. Cristea:** Writing – review & editing. **C. Croitoru:** Formal analysis, Investigation. **L. Velicu:** Formal analysis, Investigation. **V. Tiron:** Formal analysis, Investigation. **P. Prepelita:** Formal analysis, Investigation. **V. Craciun:** Formal analysis, Investigation. **C. Moura:** Resources, Investigation, Supervision, Writing – review & editing. **L. Cunha:** Resources, Supervision, Investigation, Writing – review & editing.

Declaration of competing interest

The authors declare that they have no known competing financial interests or personal relationships that could have appeared to influence the work reported in this paper.

Data availability

Data will be made available on request.

Acknowledgements

This work was supported by the Portuguese Foundation for Science and Technology (FCT) in the framework of the Strategic Funding UIDB/04650/2020, and Tunisian Ministry of Higher Education and Scientific Research. V. Craciun's work was supported by Romanian projects PCE104, PED580 and Nucleu LAPLAS VII.

References

[1] Y. Liu, M. Cheng, Z. Liu, G. Zeng, H. Zhong, M. Chen, C. Zhou, W. Xiong, B. Shao, B. Song, Chemosphere 236 (2019) 124387–124395, https://doi.org/10.1016/j.chemosphere.2019.124387.
[2] M.C. Ncibi, B. Mahjoub, M. Seffen, Bioresour. Technol. 99 (2008) 5582–5589, https://doi.org/10.1016/j.biortech.2007.10.040.
[3] X. Gong, D. Huang, Y. Liu, G. Zeng, R. Wang, J. Wei, C. Huang, P. Xu, J. Wan, C. Zhang, Bioresour. Technol. 253 (2018) 64–71, https://doi.org/10.1016/j.biortech.2018.01.018.
[4] M. Česen, T. Kosjek, E. Heath, Fate and Effects of Anticancer Drugs in the Environment, Springer, Cham, 2020, pp. 259–291.
[5] I. Velo-Gala, J.J. López-Peñalver, M. Sánchez-Polo, J. Rivera-Utrilla, Appl. Catal. B Environ. 207 (2017) 412–423, https://doi.org/10.1016/j.apcatb.2017.02.028.
[6] X. Liu, C. Chen, Mater. Lett. 261 (2020) 127127–127131, https://doi.org/10.1016/j.matlet.2019.127127.
[7] M. Ismael, Y. Wu, M. Wark, New J. Chem. 43 (2019) 4455–4462, https://doi.org/10.1039/C8NJ06507A.
[8] M. Shkir, B.M. Al-Shehri, M.P. Pachamuthu, A. Khan, K.V. Chandekar, S. AlFaify, M.S. Hamdy, Colloids Surf., A 587 (2020) 124340–124348, https://doi.org/10.1016/j.colsurfa.2019.124340.
[9] Q. Zhang, P. Cheah, F. Han, Q. Dai, Y. Yan, A. Pramanik, P.C. Ray, Ceram. Int. 45 (2019) 21851–21857, https://doi.org/10.1016/j.ceramint.2019.07.194.
[10] M.A. Fitri, M. Ota, Y. Hirota, Y. Uchida, K. Hara, D. Ino, N. Nishiyama, Mater. Chem. Phys. 198 (2017) 42–48, https://doi.org/10.1016/j.matchemphys.2017.05.053.
[11] N. Kamoun, S. Belgacem, M. Amlouk, R. Bennaceur, J. Bonnet, F. Touhari, M. Nouaoura, L. Lassabatere, J. Appl. Phys. 29 (2001) 2766–2771, https://doi.org/10.1063/1.1340003.
[12] D.A.R. Barkhouse, R. Haight, N. Sakai, H. Hiroi, H. Sugimoto, D.B. Mitzi, Appl. Phys. Lett. 100 (2012) 193904–193908, https://doi.org/10.1063/1.4714737.
[13] S. Buecheler, D. Guettler, A. Chirila, R. Verma, U. Müller, T.P. Niesen, J. Palm, A. N. Tiwari, Thin Solid Films 517 (2009) 2312–2315, https://doi.org/10.1016/j.tsf.2008.10.135.
[14] J. Herrero, J. Ortega, Sol. Energy Mater. 17 (1988) 357–368, https://doi.org/10.1016/0165-1633(88)90017-2.
[15] E. Aydin, M. Sankir, N.D. Sankir, J. Alloys Compd. 603 (2014) 119–124, https://doi.org/10.1016/j.jallcom.2014.03.064.
[16] S. Buecheler, D. Guettler, A. Chirila, R. Verma, U. Müller, T.P. Niesen, J. Palm, A. N. Tiwari, Thin Solid Films 517 (2009) 2312–2315, https://doi.org/10.1016/j.tsf.2008.10.135.
[17] S. Spiering, D. Hariskos, M. Powalla, N. Naghavi, D. Lincot, Thin Solid Films 431 (2003) 359–363, https://doi.org/10.1016/S0040-6090(03)00151-2.
[18] P. Pistor, J.M. Merino Álvarez, M. León, M. di Michiel, S. Schorr, R. Klenka, S. Lehmann, Acta. Cryst. B Struct. Sci. Cryst. Eng. Mater. 72 (2016) 410–415, https://doi.org/10.1107/S2052520616007058.
[19] Y. Bchiri, B. Tiss, N. Bouguila, R. Souissi, M. Kraini, C. Vázquez-Vázquez, K. Khirouni, S. Alaya, Mater. Sci. Semicond. Process. 121 (2021) 105294–105300, https://doi.org/10.1016/j.mssp.2020.105294.
[20] X. Yuan, L. Jiang, J. Liang, Y. Pan, J. Zhang, H. Wang, L. Leng, Z. Wu, R. Guan, G. Zeng, Chem. Eng. Jour. 356 (2019) 371–381, https://doi.org/10.1016/j.cej.2018.09.079.
[21] J. Li, Y. Ma, Z. Ye, M. Zhou, H. Wang, C. Ma, D. Wang, P. Huo, Y. Yan, Appl. Catal. B Environ. 204 (2017) 224–238, https://doi.org/10.1016/j.apcatb.2016.11.021.
[22] Y. Li, T. Li, J. Tian, X. Wang, H. Cui, Part. Part. Syst. Char. 34 (2017) 1700127–1700130, https://doi.org/10.1002/ppsc.201700127.
[23] D.P. Dutta, G. Sharma, S. Ghoshal, N.P. Kushwah, V.K. Jain, Nanotechnology 6 (2006) 235–240, https://doi.org/10.1166/jnn.2006.17937.
[24] W. Qiu, M. Xu, X. Yang, F. Chen, Y. Nan, J. Zhang, H. Iwai, H. Chen, J. Mater. Chem. 21 (2011) 13327–13333, https://doi.org/10.1039/C1JM11616A.
[25] W. Du, J. Zhu, S. Li, X. Qian, Cryst. Growth Des. 8 (2008) 2130–2136, https://doi.org/10.1021/cg7009258.
[26] S. Yang, C.Y. Xu, B.Y. Zhang, L. Yang, S.P. Hu, L. Zhen, J. Colloid Interface Sci. 491 (2017) 230–237, https://doi.org/10.1016/j.jcis.2016.12.028.
[27] Y.H. Kim, J.H. Lee, D.W. Shin, S.M. Park, J.S. Moon, J.G. Nam, J.B. Yoo, Chem. Commun. 46 (2010) 2292–2294, https://doi.org/10.1039/B922366E.
[28] L. Liu, H. Liu, H.Z. Kou, Y. Wang, Z. Zhou, M. Ren, M. Ge, X. He, Cryst. Growth Des. 9 (2009) 113–117, https://doi.org/10.1021/cg701194b.
[29] H.X. Bai, L.X. Zhang, Y.C. Zhang, Mater. Lett. 63 (2009) 823–825, https://doi.org/10.1016/j.matlet.2009.01.023.

[30] Y. Liu, M. Zhang, Y. Gao, R. Zhang, Y. Qian, Mater. Chem. Phys. 101 (2007) 362–366, https://doi.org/10.1016/j.matchemphys.2006.06.012.
[31] S. Rengaraj, S. Venkataraj, C. Tai, Y. Kim, E. Repo, M. Sillanpää, Langmuir 27 (2011) 5534–5541, https://doi.org/10.1021/la104780d.
[32] R. Souissi, N. Bouguil, A. Labidi, Sensor. Actuator. B 261 (2018) 522–530, https://doi.org/10.1016/j.snb.2018.01.175.
[33] A.S. Altowyan, J. Hakami, H. Algarni, Mohd. Shkir, Inorg. Chem. Commun. 153 (2023) 110738–110747, https://doi.org/10.1016/j.inoche.2023.110738.
[34] I.L.P. Raj, S. Valanarasu, A.B.G. Trabelsi, F.H. Alkallas, Mohd. Shkir, S. AlFaify, K. K. Saxena, Mater. Chem. Phys. 308 (2023) 128282–128291, https://doi.org/10.1016/j.matchemphys.2023.128282.
[35] D.P. Ojha, M.B. Poudel, H.J. Kim, Mater. Lett. 264 (2020) 127363–127366, https://doi.org/10.1016/j.matlet.2020.127363.
[36] Z. Zheng, J. Yu, S. Cheng, Y. Lai, Q. Zheng, D. Pan, J. Mater. Sci. Mater. Electron. 27 (2016) 5810–5817, https://doi.org/10.1007/s10854-016-4496-3.
[37] P.E. Rodríguez-Hernández, J.G. Quiñones-Galván, L. Marasamy, M. Morales-Luna, J. Santos-Cruz, J.S. Arias-Cerón, O. Zelaya-Angel, F. de Moure-Flores, Mater. Sci. Semicond. Process. 103 (2019) 104600–104606, https://doi.org/10.1016/j.mssp.2019.104600.
[38] M. Mathew, R. Jayakrishnan, P.M. Ratheesh Kumar, C. Sudha Kartha, K. P. Vijayakumar, J. Appl. Phys. 100 (2006), 33504, https://doi.org/10.1063/1.2221531.
[39] A. Kennedy, H. Ganesan, R. Marnadu, S.K. Kannan, S.I. Arockiam, M. Ubaidullah, M. Shkir, S. AlFaify, S. Gedi, Opt. Mater. 124 (2022) 111769–111777, https://doi.org/10.1016/j.optmat.2021.111769.
[40] M. Oztas, M. Bedir, Thin Solid Films 516 (2005) 1703–1709, https://doi.org/10.1016/j.tsf.2007.05.018.
[41] Y.F. Yang, M.M. Al-Jassim, S.H. Wei, Appl. Phys. Lett. 89 (2006) 181912–181914, https://doi.org/10.1063/1.2378404.
[42] J. Wang, X. Gong, J. Hai, T. Li, Vacuum 152 (2018) 132–137, https://doi.org/10.1016/j.vacuum.2018.03.015.
[43] M. Riaz, R. Zia, A. Ijaz, T. Hussain, M. Mohsin, A. Malik, Mater. Sci. Eng. C 90 (2018) 308–313, https://doi.org/10.1016/j.msec.2018.04.076.
[44] M. Mathew, C. Sudha Kartha, K.P. Vijayakumar, J. Mater. Sci. Mater. Electron. 20 (2009) 294–298, https://doi.org/10.1007/s10854-008-9591-7.
[45] P. Lin, S. Lin, S. Cheng, J. Ma, Y. Lai, H. Zhou, H. Jia, Adv. Eng. Mater. 2014 (2014) 1–4, https://doi.org/10.1155/2014/370861.
[46] N.D. Sankır, E. Aydın, M. Sankır, Int. J. Electrochem. Sci. 9 (2014) 3864–3875. https://hdl.handle.net/20.500.11851/518.
[47] S. Alhammadi, B.G. Mun, S. Gedi, V.R.M. Reddy, A.M. Rabie, M.S. Sayed, J.-J. Shim, H. Park, W.K. Kim, J. Mol. Liq. 344 (2021) 117649–117659, https://doi.org/10.1016/j.molliq.2021.117649.
[48] M.K. Salman, S. Asgary, S. Tehrani-Nasab, J. Mater. Sci. 58 (2023) 12143–12157, https://doi.org/10.1007/s10853-023-08777-w.
[49] Z. Qiu, H. Gong, G. Zheng, S. Yuan, H. Zhang, X. Zhu, H. Zhou, B. Cao, J. Mater. Chem. C 5 (2017) 7084–7094, https://doi.org/10.1039/c7tc01224a.
[50] A. Goktas, F. Aslan, B. Yeşilata, İ. Boza, Mater. Sci. Semicond. Process. 75 (2018) 221–233, https://doi.org/10.1016/j.mssp.2017.11.033.
[51] P. Kongsong, N. La-ong Srakaew, P. Phoempoon, M. Masae, L. Sikong, Mater. Sci. Forum 928 (2018) 71–76. https://doi.org/10.4028/www.scientific.net/msf.928.71.
[52] Q. Huang, J. Zhang, R. Qi, Y. Yang, F. Wang, J. Zhu, Z. Zhang, Z. Wang, Opt Express 24 (2016) 15620–15630, https://doi.org/10.1364/oe.24.015620.
[53] S. Rasool, K. Saritha, K.T. Ramakrishna Reddy, M. S Tivanov, O.V. Korolik, V. F. Gremenok, S.P. Zimin, I.I. Amirov, Adv. Nat. Sci. Nanosci. Nanotechnol. 14 (2023) 25010–25017, https://doi.org/10.1088/2043-6262/acd684.
[54] J. Lv, W. Gong, K. Huang, J. Zhu, F. Meng, X. Song, Z. Sun, Superlattice. Microst. 50 (2011) 98–106, https://doi.org/10.1016/j.spmi.2011.05.003.
[55] B. Liu, Y. Gu, W. Huang, S. Deng, S. Wang, Y. Ma, H. Wang, H. Huang, Q. Gong, T. Li, X. Shao, X. Li, H. Gong, Mater. Sci. Semicond. Process. 165 (2023) 107656–107665, https://doi.org/10.1016/j.mssp.2023.107656.
[56] B.H. Kumar, M.C. Santhosh Kumar, Mater. Sci. Semicond. Process. 111 (2020) 104983–104993, https://doi.org/10.1016/j.mssp.2020.104983.
[57] A. Timoumi, W. Zayoud, A. Sharma, M. Kraini, N. Bouguila, A. Hakamy, N. Revaprasadu, S. Alaya, J. Mater. Sci. Mater. Electron. 31 (2020) 13636–13645, https://doi.org/10.1007/s10854-020-03921-7.
[58] B. Tiss, M. Erouel, N. Bouguila, M. Kraini, K. Khirouni, J. Alloys Compd. 771 (2019) 60–66, https://doi.org/10.1016/j.jallcom.2018.08.125.
[59] A. Khorsand Zak, W.H.Abd. Majid, M.E. Abrishami, R. Yousef, Solid State Sci. 13 (2011) 251–256, https://doi.org/10.1016/j.solidstatesciences.2010.11.024.
[60] V. Bilgin, S. Kose, F. Atay, I. Akyz, Mater. Chem. Phys. 94 (2005) 103–108, https://doi.org/10.1016/j.matchemphys.2005.04.028.
[61] B. Tiss, M. Benfraj, N. Bouguila, M. Kraini, S. Alaya, D. Cristea, C. Croitoru, V. Craciun, D. Craciun, P. Prepelita, I.-L. Velicu, V. Tiron, C. Moura, L. Cunha, Mater. Chem. Phys. 270 (2021) 124838–124849, https://doi.org/10.1016/j.matchemphys.2021.124838.
[62] Y. Zhang, E.K. Stefanakos, D.Y. Goswami, Built. Environ. 61 (2013) 188–196, https://doi.org/10.1016/j.buildenv.2012.12.018.
[63] B. Tiss, Y. Moualhi, N. Bouguila, M. Erouel, M. Kraini, S. Alaya, S. Aouida, C. Vázquez–Vázquez, C. Moura, L. Cunha, J. Mater. Sci. Mater. Electron. 32 (2021) 4568–4580, https://doi.org/10.1007/s10854-020-05198-2.
[64] P. Kongsong, N. La-ong Srakaew, P. Phoempoon, M. Masae, L. Sikong, Mater. Sci. Forum 928 (2018) 71–76. https://doi.org/10.4028/www.scientific.net/msf.928.71.
[65] R.K. Kothandaraman, Y. Jiang, T. Feurer, A.N. Tiwari, F. Fu, Fu Fan, Small Methods 4 (2020) 2000395–2000450, https://doi.org/10.1002/smtd.202000395Citations.
[66] R. Sahebi, J. Photochem. Photobiol. Chem. 401 (2020) 112750–112751, https://doi.org/10.1016/j.jphotochem.2020.112750.
[67] E.A. Davis, N.F. Mott, Phil. Mag. 22 (1970) 903–922, https://doi.org/10.1080/14786437008221061.
[68] Y.H. Yang, X.Y. Chen, Y. Feng, G.W. Yang, Nano Lett. 7 (2007) 3879–3883, https://doi.org/10.1021/nl071849h.
[69] C. An, S. Peng, Y. Sun, Adv. Mater. 22 (2010) 2570–2574, https://doi.org/10.1002/adma.200904116.
[70] Z. Wu, X. Yuan, G. Zeng, L. Jiang, H. Zhong, Y. Xie, H. Wang, X. Chen, H. Wang, Appl. Catal., B 225 (8) (2018) 8–21, https://doi.org/10.1016/j.apcatb.2017.11.040.
[71] J. Feng, Z. Yang, S. He, X. Niu, T. Zhang, A. Ding, H. Liang, X. Feng, Chemosphere 212 (1) (2018) 14–124, https://doi.org/10.1016/j.chemosphere.2018.08.070.
[72] N.C. Castillo, A. Heel, T. Graule, C. Pulgarin, Appl. Catal. B Environ. 95 (2010) 335–347, https://doi.org/10.1016/j.apcatb.2010.01.012.
[73] A. Iborra-Torres, M. Huš, K. Nguyen, A. Vamvakeros, M.T. Sajjad, S. Dunn, M. Mertens, S. Jacques, A.M. Beale, B. Likozar, G. Hyett, S. Kellici, V. Middelkoop, Mater. Adv. (2023), https://doi.org/10.1039/d2ma01076c.
[74] Y. Ben Salem, M. Kilani, N. Kamoun, Res. Phys. 10 (2018) 706–713, https://doi.org/10.1016/j.rinp.2018.02.078.